Optically interrogated MEMS pressure sensor array

Lukas Prochazka[1], Alexander H. Meier[2], Thomas Roesgen[3]

1: Institute of Fluid Dynamics, ETH Zurich, Switzerland, prochazka@ifd.mavt.ethz.ch
2: Institute of Fluid Dynamics, ETH Zurich, Switzerland, meier@ifd.mavt.ethz.ch
3: Institute of Fluid Dynamics, ETH Zurich, Switzerland, roesgen@ifd.mavt.ethz.ch

Abstract A novel pressure measurement technique is developed with the objective to simplify wind tunnel investigations while providing a full field surface pressure measurement capability with very high measurement performance. An array of silicon diaphragm micro-resonators acts as pressure sensing element. The pressure distributions are recorded by measuring the diaphragm's resonance frequency by interferometric means. Dependent on the quasi-static deflection caused by a pressure load the resonance frequency varies with an average pressure sensitivity of 3 Hz/Pa in a frequency range between 30 and 150 kHz (dependent on the structural vibration mode). A smart-pixel CMOS camera, a narrow band acoustic noise excitation and a specific sensor surface structure allow for the interrogation of a large number of sensors in parallel and without the need for alignment between sensor and detector.

1. Introduction

During aerodynamic and mechanical load performance surveys in wind tunnel testing it is often desirable to obtain the surface pressure on a specific component of the investigated model with high spatial resolution, good measurement accuracy and low uncertainty. Despite its importance, to measure the static pressure only the pressure tap method tends to be used in commercial and industrial wind tunnel facilities. This technique, where the transducers are linked by tubes to the measurement locations, provides high measurement performance but is also very costly due to the required mechanical and pneumatic interfacing in the test model. The application of pressure sensitive paints for low speed testing at atmospheric pressure conditions is often inaccurate due to the low sensitivity and large temperature cross-sensitivity (Liu et al. 2005, Airaghi 2006).
The objective of the present work is to develop a technique to measure the static pressure distribution with a performance (i.e. high accuracy, low measurement uncertainty) comparable to the pressure tap system but with less handling and installation requirements. The requirements on the measurement performance are summarized in Table 1.

Table 1 Required measurement performance

Temporal resolution	≈ 1 Hz
Spatial resolution	> 5 mm
Measurement range	< 10 kPa
High sensitivity	0.2% FS or 20 Pa
Low measurement uncertainty (drift, cross sensitivity, …)	

Based on a previous study, a concept which is regarded as the best suitable measurement technique for the target application was defined (Prochazka et al. 2005). It is based on very small, passive MEMS pressure sensor dies (plate resonators) which are mounted directly on the model surface and are optically interrogated using a highly sensitive active pixel CMOS lock-in detector.

The present paper describes the current status of sensor design, fabrication (first prototype) and experimental tests to verify the sensor's performance. An experimental feasibility study regarding the whole measurement setup is presented as well.

2. Method

The pressure sensing system is based on the optical interrogation of an array of passive MEMS pressure sensors (silicon diaphragms) which are embedded in a thin (0.3 mm) Kapton foil. To allow for differential (gauged) pressure sensing operation and thus highest sensitivity a pneumatic tubing system is integrated into the Kapton foil and interconnects the individual sensor cavities (Fig. 2.2). Using a pressure controller linked to the foil by a single tube, the pressure in the cavity (back pressure) is set to a constant reference value of about 100 mbar below ambient pressure which enables signed pressure measurement. In case of small-scale models, where the foil could alter the flow characteristics, the sensor foil may be recessed in a milled slot in the model surface.

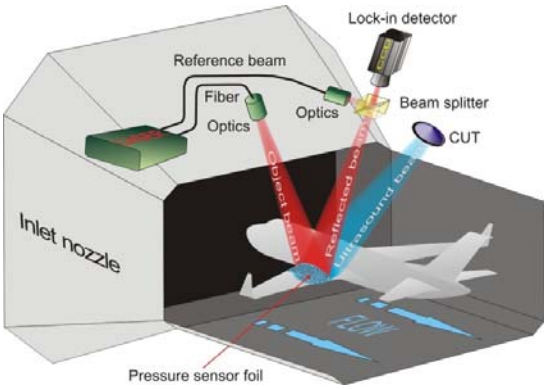

Fig. 2.1 Measurement setup including the remote imaging interferometer and the ultrasound transducer

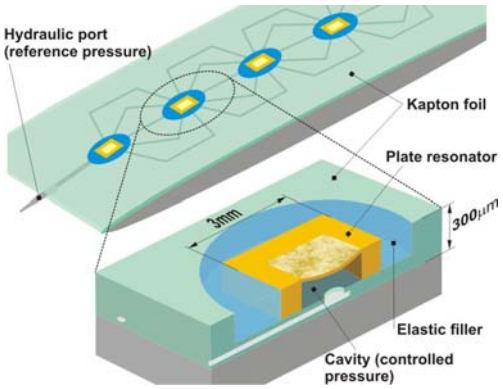

Fig. 2.2 Sensor design and packaging within a thin structured Kapton foil

As a measure for the applied pressure the resonance frequency of the clamped silicon plate is used which depends on its quasi-static deflection and thus on the applied pressure. The readout is achieved in a two-stage configuration. First, an ultrasound transducer (emitting band-limited "pink" noise) excites the diaphragms into free oscillation. The actual resonant vibration responses of the individual sensing elements are then measured with an imaging interferometer. This device is based on a highly sensitive, "active-pixel" CMOS camera (HELIOTIS, Switzerland) that works as a full field lock-in detector with a spatial resolution of 144 x 90 pixels (> 10^4 measurement points) (Beer et al. 2005). It can resolve signal frequencies up to 250 kHz while providing very strong background (i.e. static image) rejection and a frame rate of 6 kHz. The modulated optical signal with the particular frequency arises due to the interference between the object and reference beams. A "digital" frequency output signal (i.e. basically independent of analog levels) allows a more accurate and robust interrogation of the sensor compared with direct displacement measurement by optical means especially if - as in the present setup - a wireless and remote readout capability of about 2 meters is considered.

An optical interrogation on curved surfaces and without a precise alignment between sensor and detector requires a diaphragm surface with an optically diffuse scattering property. The imposed roughness on the initially highly reflective silicon wafer surface consists of highly dense and randomly distributed tiny grooves with an average depth of approximately 100 nm (chapter 4).

Using ultrasound allows the excitation of several sensing devices in parallel without altering the sensing behavior due to heating as would be a problem with laser excitation or due to specific

actuators as in the electrical case. The difficulty associated with this excitation principle is mainly related to the high losses caused by strong attenuation of ultrasound in air and the less stable and

Fig. 2.3 CUT (SensComp, Inc.) used in the present setup and its power supply (self-made). Transducer diameter ≈ 40mm

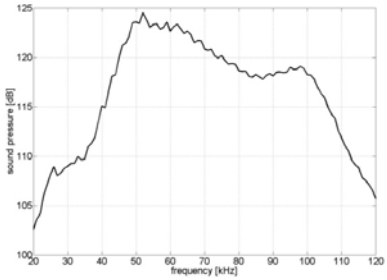

Fig. 2.4 Transmitting characteristic of the CUT (SensComp, Inc.) operated with 200 $Volt_{DC}$ and 350 $V_{AC\ p\text{-}p}$ (Sound pressure measured at 1m from transducer)

non-uniform transmitting characteristics of an ultrasound transducer (UT) compared with electrical or optical excitation. Therefore a high power capacitive UT is used for the present measurement setup (SensComp, Inc.). Advantages of CUTs are their high transmitting efficiency in air in combination with a wide bandwidth and the simple design that is reflected in their low cost (Manthey et al. 1992, Rafiq et al. 1991).
The present CUT has a large active diaphragm of about 40 mm and provides a sound pressure of up to 120 dB (at 1 m from transducer) in a wide frequency range between 50 and 100 kHz (Fig. 2.4). Experimental tests have shown that sufficiently strong excitation is possible even up to 150 kHz using the mentioned CUT (chapter 5). An important goal during sensor design and development is to minimize the damping behavior of the plate resonator in order to reduce the effects of the unstable transmitting characteristics of a CUT.

3. Sensor Design

The main component of the sensor unit is the resonator which is basically a thin clamped plate and thus similar to ordinary MEMS pressure sensors. The only difference is that the sensor in the present work is completely passive and thus no electronic elements or wiring have to be implemented during fabrication. The frequency operating range and the pressure sensitivity are mainly defined by the size and the thickness of the diaphragm. In a previous survey (Prochazka et al. 2008) the optimum diaphragm size and thickness were determined based on criteria such as maximum average pressure sensitivity and requirements on the spatial resolution (maximum sensor size). The influence of environmental vibrations on the sensing behavior and the interaction of acoustic noise with the boundary layer on a wind tunnel model were considered as well. The resonance frequency characteristic was determined using simple semi-empirical formulas without considering the coupling between the diaphragm and the cavity and tubing system or the open surroundings on the outer side of the diaphragm. The optimum diaphragm size is around 1.5 mm with a thickness below 10 μm. A minimum thickness constraint (≈ 6 μm) is mainly given by fabrication issues and mechanical strength and durability concerns. The corresponding frequency operating range is located between 50 and 100 kHz. The overall chip size of the final sensor should not exceed 2.5 mm and a height of 200 μm. As material single crystal silicon (SCS) is chosen due to its excellent mechanical properties such as a strength comparable to that of steel and an elastic behavior up to fracture, leading to minimal hysteresis phenomena (Tudor 1997). A thin Kapton foil (0.3 mm thick) is used as flexible support for the sensor array. A pneumatic tubing system integrated in the foil (inscribed using a laser structuring technique) interconnects the individual pressure sensor cavities and thus provides the possibility to control the reference pressure (back

pressure) using a fast pressure controller. An experimental survey to identify the optimum tubing system design is currently ongoing. The micro channels are approximately 50 μm deep, 200 μm wide and several millimeters long (dependent on the separation distance between the individual sensing elements). To minimize thermal and mechanical stresses due to the bond between the sensor and the support (foil) an elastic silicon filler material is used.

4. Sensor Fabrication

The fabrication of the prototype relies basically on deep dry etching from the rear side of a SOI (Silicon On Insulator) wafer to obtain a uniform and reproducible diaphragm thickness (Fig. 4.2). The insulator of a SOI (i.e. the 1 μm thick oxide layer) acts as a precise etch stop. Due to the highly anisotropic etching characteristics of common dry etching processes the sensor cavity features vertical walls and thus the overall chip size is minimized compared to the results obtainable with wet etching techniques (54.7º walls) (Fig. 4.1). The current prototype features not the required overall height of 200 μm but is 400 μm high due to better handling capabilities during fabrication. Four different diaphragm sizes between 1.4 and 2 mm with a diaphragm thickness of 7 μm were manufactured. The overall chip size is kept constant at 4.5 mm for all chips to assure a strong support of the diaphragm. The minimum chip size has yet to be evaluated in a separate study.

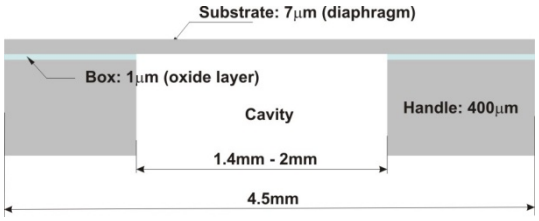

Fig. 4.1 Sensor layout of the prototype

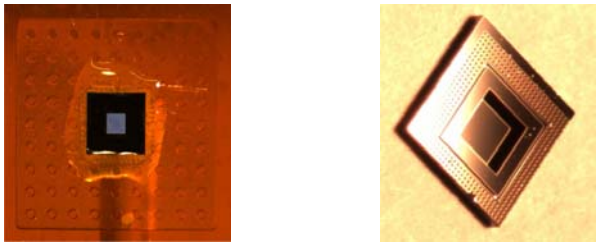

Fig. 4.2 Sensor with roughened top diaphragm surface and inserted in a 0.25 mm thick, laser structured Kapton foil (left), Exposed rear side of the sensor with cavity and rear side of the diaphragm (right)

Below, the fabrication process for making a thin diaphragm optically rough is described more in detail. Besides the requirements on the optical properties (highly diffuse scattering, low dispersion and diffraction) the structural impact has to be considered as well. The maximum roughness height is therefore restricted to approximately 100 nm in order to prevent a degradation of the fracture strength of single-crystal silicon (SCS) (Henning et al. 2004). It is also required that the roughness is directly implanted into the silicon and not created by deposition of different materials onto the silicon surface so as to prevent thermal stresses due to the bimetal effect.
Wet etching of SCS ({100}-wafer) is usually orientation dependent (i.e. anisotropic) and thus produces grooves with 54.7º walls with respect to the wafer surface (Fruehauf 2005). If two opposing walls meet each other the etching slows down considerably. This so called geometrical etch stop can be used to better control the etch depth especially if short etching is applied. To utilize the mentioned etch stop technique the etch windows within the oxide mask have to be approximately of the same size as the roughness height. With common optical photolithography processes (UV light) the limiting features size is 1 micron (Helbert 2001). Using e-beam lithography features far smaller than 1 micron can be transferred to the oxide mask but the writing process is sequential and thus the transfer of a high number of features becomes very time consuming. Therefore a novel fabrication process for an efficient roughening of a silicon surface was developed in the present work. The process is based on thin film deposition of poly-silicon and wet etching in TMAH (Tetramethylammonium Hydroxide) and is described below.

During the first processing step the area on the wafer is predefined where a rough surface is to be produced. For that the 500 nm thick oxide layer is structured using common photolithography and dry etching processes. The wafer is again oxidized to obtain an additional 0.1 nm thick oxide film which acts as the mask for the final wet etching process. The deposition of poly-silicon is performed in a LPCVD (Low Pressure Chemical Vapor Deposition) furnace at 500 ºC for 25 min (Fig. 4.3a). During the subsequent *in situ* annealing under ultrahigh vacuum (510 ºC, 60 min) the formation of hemispherical grained silicon (HSG) takes place (Sallese et al. 2000, Watanabe et al. 1992) (Fig. 4.3b). During the nucleation process the poly-silicon is consumed in the vicinity of a HSG and thus is partially or completely removed (Fig. 4.3c and g).

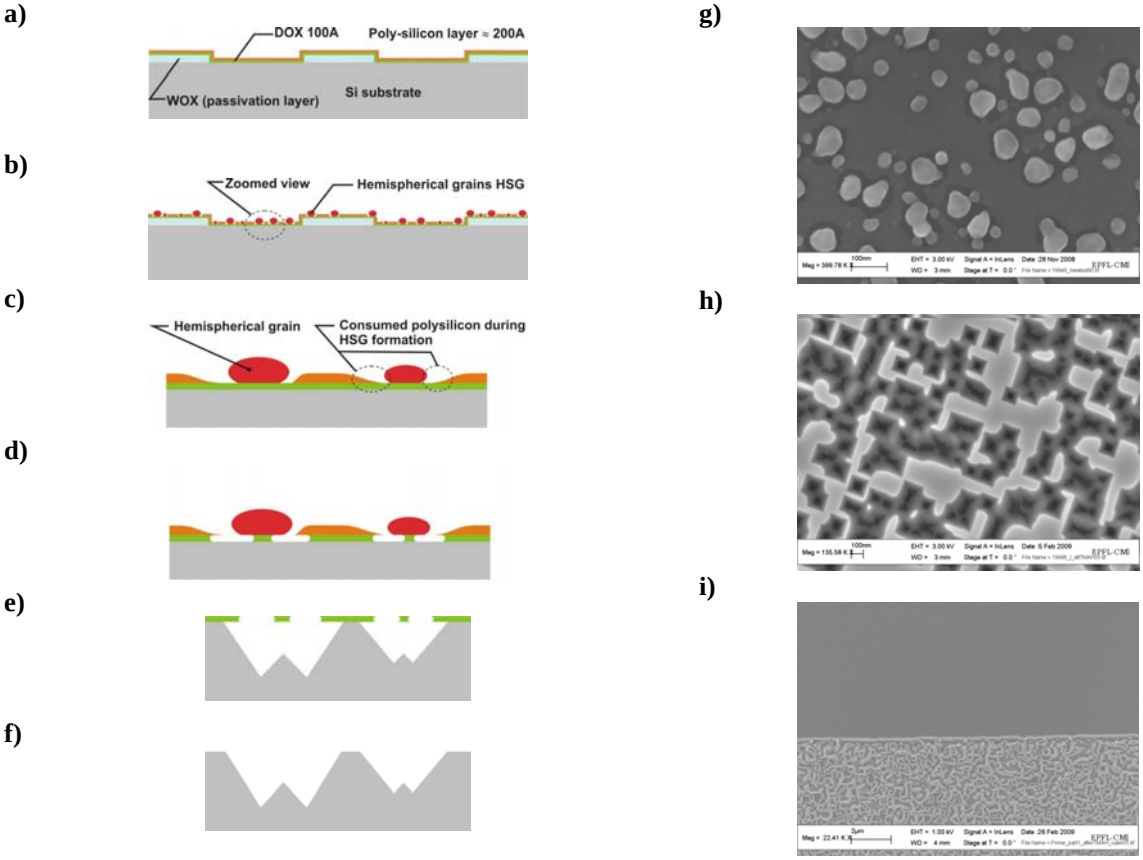

Fig. 4.3 Fabrication process: Surface roughening (a-f), g) SEM of the HSG distribution after the annealing process, h) SEM of roughness topography with overlying mask (oxide film) after TMAH etching, i) SEM of the roughened top diaphragm surface (lower part) and the highly specular silicon surface of the outer region

The subjacent oxide film (DOX100) is released within these areas and is removed in BHF (Buffered Hydrofluoric Acid) (dip time 15 sec at 25 ºC) (Fig. 4.3e and h). The oxide film becomes porous with submicron openings (< 100 nm) which allow the non-uniform wet etching of silicon in TMAH 5% (50ºC, 5 min) (Fig. 4.3f and i).

The rough surface is composed of a random and dense arrangement of tiny grooves with a maximum size of about 100nm (estimate is based on the groove size) (Fig. 4.3i). Despite the roughness height in the sub-wavelength range of visible light the scattering property is surprisingly high. If illuminated with white light the rough surface appears white and thus dispersion effects should be small (Fig. 4.2). If illuminated with coherent light no diffraction phenomena were observed during experimental tests. A detailed experimental study is under way to corroborate the mentioned observations with quantitative data (reflectivity measurements, etc.).

5. Experimental verification of the plate resonator behavior

In order to verify the pressure sensing behavior of the newly fabricated resonators experimental tests were carried out in a temperature controlled test cell (Fig. 5.1). The temperature was set and controlled using a Peltier heater and two heat exchangers between 20 and 35 ºC (accuracy < 0.02 K). The sensor was loaded by adjusting and controlling the pressure in the cavity behind the diaphragm (back pressure) using a fast and highly accurate pressure controller (PACE 5000, GE Sensing) (accuracy < 10Pa). The pressure within the test cell was kept at ambient conditions. The measurement configuration differs from the actual one where the back pressure is kept constant at a certain level and the ambient pressure varies but it simplifies the measurement procedure considerably because only one pressure level has to be controlled. The influence of the reversed pressure boundary conditions on the sensing behavior is assumed to be negligible but remains to be verified. The sensor holder is designed with the objective to allow a simple pneumatic access to the sensor cavity and a rapid mounting within the test cell. Its upper part, a 125 µm thick Kapton foil, exhibits a laser structured slot into which the sensor is glued using a silicon filler material. The bottom part is made out of acrylic glass (6 mm thick) and includes a 30 mm large and 50 µm deep settling chamber which is connected to the sensor cavity using ten 2 mm long micro channels (Fig. 4.2). The glass holder is structured by mechanical milling.

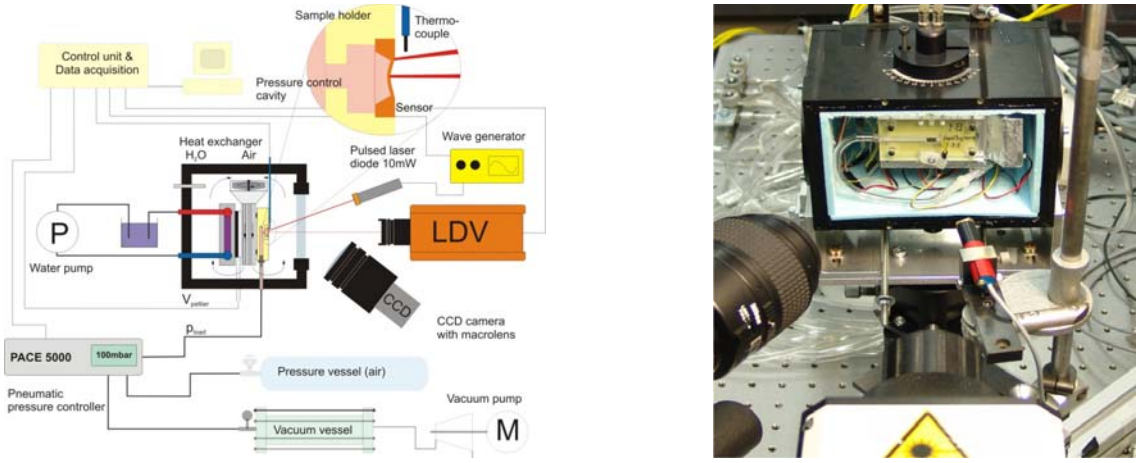

Fig. 5.1 Experimental setup for the investigation of the new fabricated sensor (optical excitation)

Due to the hermetically sealed cell and limited internal space it was not possible to combine acoustic excitation and temperature control inside the cell. Instead an external, pulsed laser diode (Flexpoint 10mW, Laser Components GmbH) was used to heat the diaphragm locally and thus to generate mechanical stresses which excite the diaphragm into vibration with a certain excitation frequency. The dynamic amplitude was then measured with a laser vibrometer (LDV, OFV-551, Polytec GmbH) from outside of the test cell. During a test run the excitation frequency was swept across the range of interest with steps of 20 Hz in the neighborhood of the resonance peak. The resonance frequency was then found by locating the maximum amplitude. Compared to acoustic noise excitation the monochromatic optical excitation allows a more precise analysis of the oscillation behavior, including the damping behavior (Q-factor) and interference phenomena due to fluid structure coupling. The Q-factor is inversely related to the damping of an oscillator and is determined based on the amplitude spectrum ($Q = f_{res}/\Delta f_{3dB}$) (Stemme 2001).
During tests with acoustic excitation the test cell was kept open. The distance between sensor and CUT was set at 1m. The diaphragm vibration induced by narrow band acoustic noise is recorded using the vibrometer, and the frequency was determined based on a FFT-algorithm (Fast Fourier Transform). All existing structural vibration modes within a frequency range between 30 and 150

kHz (restricted by the operating range of the CUT) were considered during the present survey. Except for the smallest diaphragm (1.4 mm) (only the first two modes can be excited by the CUT) the corresponding modes are the fundamental symmetric mode (1,1) and the two subsequent asymmetric modes (1,2) and (2,2) (Fig. 5.2). Dependent on the considered mode the operating frequency band of the CUT was adapted to the corresponding frequency range (≅ 12kPa pressure range) to minimize any potential cross coupling between individual modes
In Figure 5.2 operating lines (resonance frequency as function of the pressure load) representing the three mentioned vibration modes for a 1.4 mm and a 1.8 mm diaphragm are shown. The solid lines represent the characteristics if optical excitation is used and the markers show the sensor behavior if the sensor is driven by acoustic noise excitation. As mentioned before the 3rd mode (2,2) cannot be excited on the smallest diaphragm with the existing CUT. Furthermore numerical results (ANSYS) from a modal analysis for a clamped plate vibrating in vacuum are plotted (dashed lines).

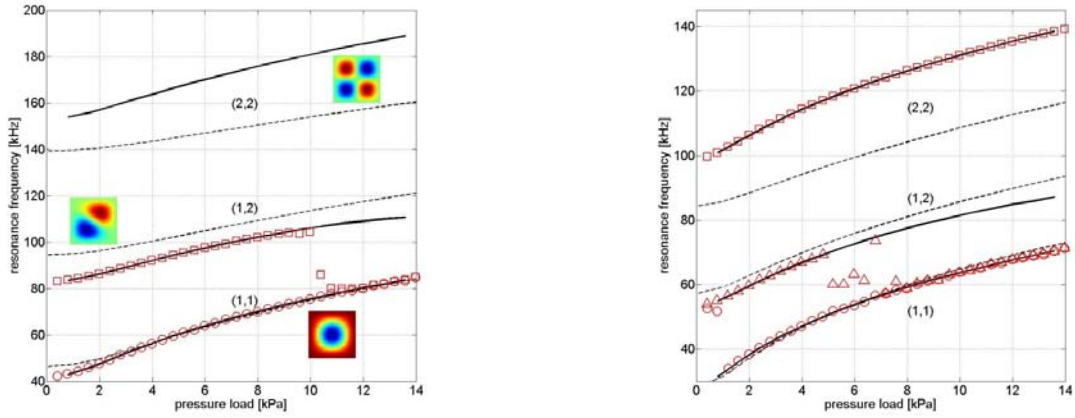

Fig. 5.2 Operating lines for the 1.4mm (left) and 1.8mm large diaphragm and for the 3 structural modes, solid lines: optical excitation, markers: ultrasound excitation, dashed lines: numerical simulations (ANSYS)

Obviously, the diaphragm size has a strong influence on the operating frequency range but only little impact on the pressure sensitivity. If the 1st and the 3rd mode are considered, the resonance frequency varies by approximately 40 kHz over a pressure range of 14 kPa, and thus an average pressure sensitivity of almost 3 Hz/Pa is achieved. The second mode is less sensitive in particular at higher pressure loads (average pressure sensitivity ≈ 2 Hz/Pa).
Considering the operating frequency the 1st and the 2nd mode start to overlap already for loads higher than 5 kPa (larger diaphragm). As a consequence the 2nd mode cannot be identified within this region if the resonator is driven by ultrasound. The 1st mode seems to be more receptive to sound waves than the 2nd one. Between the 2nd and the 3rd mode no overlap exists and thus the latter one can be detected over the whole operating range of the sensor. The agreement between numerical simulations and experiment is best for the 1st mode. The simulation predicts higher resonance frequencies for the 2nd and much lower resonance frequencies for the 3rd mode. Possible reasons for that are discussed later in this chapter.
Figure 5.3 shows the damping characteristics of the sensor expressed by the quality factor. Three different sensor sizes (1.4, 1.6 and 1.8 mm) are considered in that context. The 1st mode is strongly damped in particular for the largest diaphragm. The Q-factor is well below 100 and decreases slightly with increasing load (or frequency). An unloaded diaphragm vibrating in the 2nd mode shows Q-factors up to 300 but the damping increases strongly with increasing load (or frequency). The influence of the diaphragm size on the damping seems to be opposite to the 1st mode if the damping level at a particular pressure load is considered (Fig. 5.3 left). This behavior changes if the frequency becomes the dependent parameter (Fig. 5.3 right).
The damping characteristic of the 3rd mode differ from those of the two first modes. At first the Q-factor is well above 100 across the whole operating range, then it starts increasing with increasing

pressure load (or frequency) and finally the diaphragm size has an opposite effect on the damping if the frequency is considered as the dependent parameter. If the Q-factor characteristics of all considered modes are plotted over the frequency a tendency towards a minimum Q-factor at a certain frequency or within a certain frequency range is apparent (Fig. 5.3 right). The corresponding discussion follows later in this chapter.
In Figure 5.4 the influence of damping on the measurement uncertainty is shown. It is expressed as the standard deviation of resonance frequency based on 20 consecutive measurements using acoustic noise excitation. For Q-factors higher 100 the frequency can be determined using an standard FFT algorithm with an uncertainty of approximately 100 Hz which is close to the required 60Hz (required pressure sensitivity 20Pa).

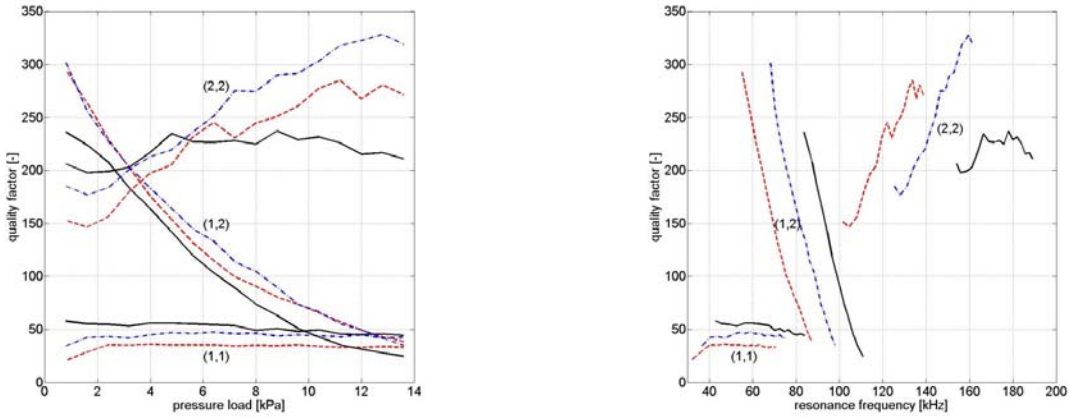

Fig. 5.3 Damping characteristics (Q-factor) of the resonator, shown as function of the pressure load (left) and the frequency (right). Considered are the first 3 structural modes and 3 different diaphragm sizes: 1.4mm (solid), 1.6mm (dash-dot) and 1.8mm (dashed)

The experimental tests confirmed the expected behavior of a plate resonator if one considers the good agreement between numerical prediction and experiment for the 1st mode. The fact that the first mode is more damped by sound radiation compared with the higher asymmetric structural modes was confirmed as well (Wallace 1972). On the other hand the tests raised open questions regarding the big discrepancy between simulation and experiment for the 3rd mode and the abnormal damping characteristics of this mode compared with the 1st and 2nd ones. It is speculated that the fluid-structure coupling on both sides of the diaphragm has a stronger effect on the plate oscillation than initially expected. Therefore the effect of the free surroundings on the outer side and the effect of the cavity and the tubing system on the back side of the diaphragm have to be analyzed more in detail.
The coupling between a vibrating plate and the open surroundings (no flow) imposes a damping but also a loading (added mass) on the structure. Damping is caused by radiation of sound energy into the fluid and loads by the oscillating movement of the fluid in the vicinity of the diaphragm (Crocker 1998). The radiation losses are basically dependent on the fluid properties, the size of the vibrating structure and the surface velocity distribution (frequency and modal shape) and are usually represented as a radiation efficiency (ratio between the radiated power of the considered structure and that of a rigid piston of the same size). Figure 5.5 shows the radiation efficiency for the first three modes of a clamped square plate with a size of 1.4 mm (solid line) and 1.8 mm (dashed line). The data were determined by solving numerically (Matlab) the Rayleigh integral (Lemmen et al. 1996). The operating range of the corresponding plate resonator is represented by a thick solid line. The 1st mode is almost one order of magnitude more damped than the 2nd mode and thus is not only a good radiator but also a good receiver for the incoming sound. That could explain why the 2nd mode cannot be detected within the overlapping frequency region between the 1st and 2nd mode. The 3rd and the 2nd mode are more or less equally damped if the corresponding frequency operating range is considered. Both observations have been confirmed experimentally. For the

considered modes the radiation efficiency increases with increasing frequency and increasing diaphragm size. This is confirmed experimentally for the two first modes but not for the 3rd one.
The fluid loading effect can be considered as an added mass which reduces the resonance frequency depending on the same parameters as the radiation losses (Crocker 1998). Within the parameter range defined by the present sensors and the working fluid (air) the frequency shift is small and can be regarded as constant over the considered frequency range. According to Wu (2009) the added mass shifts the resonance frequency by approximately 2% for the 1st mode (diaphragm size 1.8mm). For the 2nd and 3rd mode the frequency shift is less than 1%. The observed discrepancy between the numerical results and the experiment regarding the 3rd mode is more than 20% and thus cannot be fully explained by the fluid loading effect.

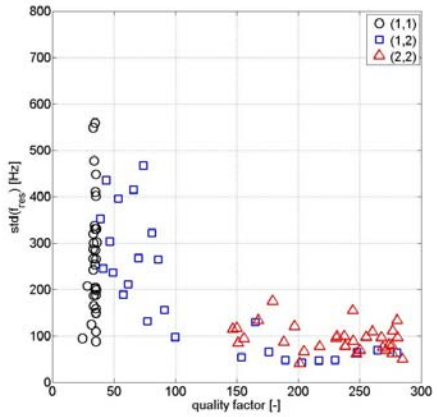

Fig. 5.4 Influence of damping on the measurement uncertainty of resonance frequency determination if ultrasound excitation is applied

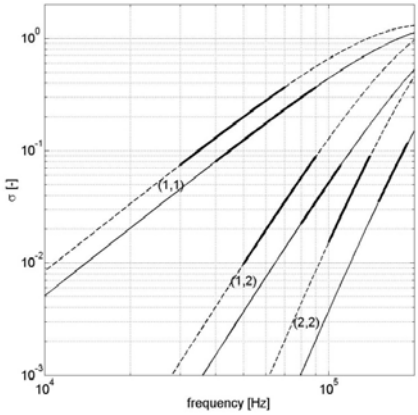

Fig. 5.5 Radiation efficiency as function of the frequency. Considered are the first 3 structural mode of a clamped square plate with a size of 1.4mm (solid) and 1.8mm (dashed)

Fluid and acoustic phenomena caused by the fluid-filled cavity which is coupled to the rear side of the diaphragm may influence the vibration behavior of the resonator. These may be acoustic resonance effects, dissipative phenomena like squeeze film damping and added mass or stiffness effects. In order to estimate the importance of the latter three mentioned effects basically one dimensionless parameter, the shear wave number s is used. The shear wave number represents the ratio between the inertial and viscous forces (eq. 5.1).

$$s = h\sqrt{\frac{\rho_0 \omega}{\mu}} \qquad (5.1)$$

$$f_{(ijk)} = \frac{c_0}{2}\sqrt{\left(\frac{i}{a}\right)^2 + \left(\frac{j}{b}\right)^2 + \left(\frac{k}{h_c}\right)^2} \qquad i,j,k = 0,1,2,\ldots \qquad (5.2)$$

ρ_o represents the air density, ω the frequency and μ the dynamic viscosity. For a cavity with a height of 400 µm the shear wave number varies between 40 and 100 for frequencies between 30 and 150 kHz. According to Beltman et al. (1998) the damping coefficient due to viscous effects is well below 1% and does not change considerably with increasing shear wave number for $s > 50$. Therefore, the abnormal damping behavior of the 3rd mode should not be caused by viscous effects within the cavity.
Added mass effects occur only for asymmetric modes where no change in cavity volume is induced and therefore the air is pumped back and forth (Beltman et al. 1998). For symmetric modes (e.g. (1,1)) the change in cavity volume induces an added stiffness effect and therefore the resonance frequency increases with decreasing cavity height. To quantify these two effects numerical simulations were performed using the FEM software COMSOL Multiphysics. The diaphragm was modeled using shell elements and was coupled to the acoustic model (cavity) by imposing pressure boundary conditions on the structural side and acceleration boundary conditions on the acoustic side. On the remaining cavity walls hard wall boundary conditions were imposed. The resonance

frequencies were determined based on a time-harmonic analysis without including any damping. For a cavity with a height of 400 μm and at ambient conditions the resonance frequency of the 1st mode increases by approximately 3% and decreases by less than 1% for the 2nd and 3rd mode compared with a diaphragm vibrating in vacuum.
Acoustic resonance effects are considered by estimating the acoustic modes in a closed, fluid-filled cavity (eq. 5.2) (Blevins 1987). The size of a rectangular cavity is described by the parameters a and b, its height by h_c and c_o represents the speed of sound in air (c_o = 343m/s). As can be seen in Figure 5.3 the damping characteristics of all considered modes tend to a minimum value at frequencies which are in good agreement with the fundamental acoustic mode of a closed fluid filled cavity (Table 5).

Table 5 Fundamental acoustic mode in a closed fluid-filled cavity (square base area)

	a = 1.4 mm	a = 1.6 mm	a = 1.8 mm
$f_{(100)}$ [kHz]	122.54	107.2	95.31

The strongly increasing damping with increasing frequency for the 2nd mode and the abnormal damping behavior of the 3rd mode may thus be explained by destructive interference between the structural and the acoustic cavity mode. A cavity design with slanted walls could probably reduce this interference effect, but would have to be validated with further numerical simulations and in experimental tests with newly designed sensors.
The aforementioned large discrepancy between experiment and numerical simulations in the operating frequency range of the 3rd mode is considered not yet explained. For the structural part of the system uncertainties regarding the effect of the rough surface on the oscillation behavior may have to be clarified. Further tests are scheduled where the particular mode shape is to be visualized using a microscopic vibrometer system.

6. Feasibility test: Full-Field Optical Interrogation

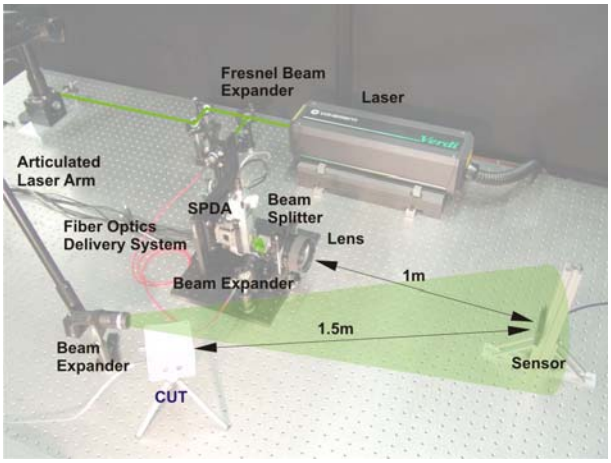

Fig. 6.1 Setup of the full-field interrogation system

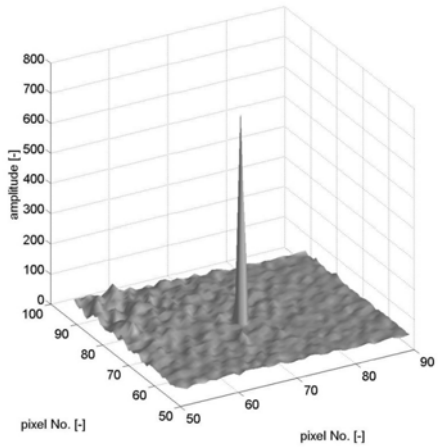

Fig. 6.2 Demodulated image (lock-in amplitude) obtained from the SPDA at resonance operation and a pressure load of 45 mbar (only a cutout of the detector array is shown)

To demonstrate the feasibility of parallel interrogation of a large number of sensors an experiment was setup where the plate resonator is interrogated using the "active-pixel" CMOS camera (SPDA) described in chapter 2. For the excitation of the resonator narrow band acoustic noise was used. From a distance of approximately 1 m and with a standard lens 4 pixels of the detector array (144 x

90 pixels) are registering the diaphragm signal (Fig. 6.2). The ultrasound transducer (CUT) was placed at a distance of 1.5 m from the sensor. Its power supply was fed with narrow band electrical noise (f_{band} 40 kHz to 100 kHz). The source beam of a CW laser (Coherent Verdi V5, λ_0 = 532 nm, output power 1 W) is split into two parts using a Fresnel beam sampler (Fig. 6.1). The object beam containing 95% of the power is expanded to cover a target scene of around 0.4 m x 0.4 m. The reference beam is redirected towards the camera using a fiber optic delivery system. A collimator expands the reference beam to cover the detector area. A beam splitter is used to mix the light from the scene and the light from the reference beam. Due to interference the result of this superposition is a harmonic, intensity -modulated signal superimposed on a constant offset. The demodulation of the ac signal is based on a dual phase lock-in detection on the pixel level. During the experiment the resonator was loaded by setting and controlling the back pressure between 30 mbar and 115 mbar (5 mbar steps) below the ambient value using the pressure controller (PACE5000, GE Sensing).
The demodulation frequency of the SPDA was swept from 50 kHz to 80 kHz in 100 steps (300 Hz per step). A total averaging over 200 measurements was performed per run (constant pressure load). During post processing the raw data is first analyzed to locate the pixel cluster which corresponds to the diaphragm (Fig. 6.2). After that an estimate of the resonance frequency is determined based on the corresponding pixel data (peak detection). Finally the raw data within an interval of 8 kHz around the resonance frequency is fitted using the least- squares method with a Gaussian profile (Fig. 6.3). The final resonance frequency is extracted using a peak detection on the Gaussian fit. Figure 6.4 compares the operating lines of the resonator (1st mode) based on the two discussed interrogation methods (vibrometer & optical excitation vs. SPDA & acoustic noise excitation). The

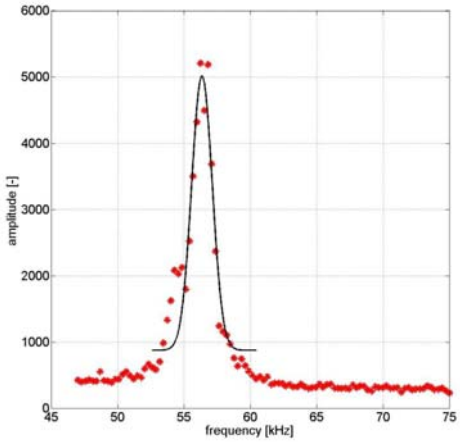

Fig. 6.3 Signal amplitude after lock-in detection on 1 pixel (72,20), Gaussian fit within an interval of 8kHz (solid line)

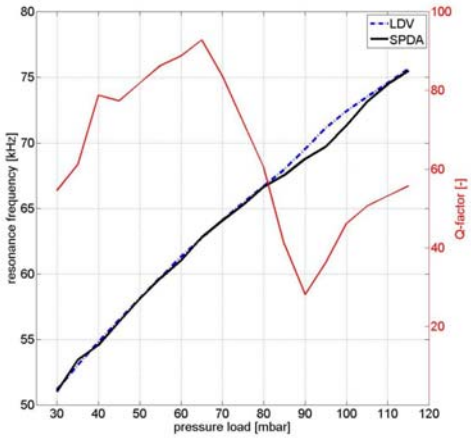

Fig. 6.4 Operating line of the resonator system using the single point (LDV) and the full-field (SPDA) interrogation method. The Q-factor characteristic (red) is based on LDV measurements and optical excitation

two methods show a very good agreement in the pressure load range between 30 and 80 mbar but diverge considerably between 80 and 110 mbar. The deviation goes along with the drop in Q-factor below 50 within the mentioned pressure load range. Due to this strongly damped oscillation behavior the amplitude at resonance is too small to generate sufficiently large signals on the detector. It has to be mentioned that the operating line in Figure 6.4 is based on tests using an older sample holder design and thus differs from the sensor characteristics shown in chapter 5.

7. Conclusion

The prototype of the diaphragm resonator shows the expected measurement performance in terms

of operating resonance frequency and pressure sensitivity. The roughened diaphragm top surface permits the optical interrogation of the resonator without the need for special alignment between sensor and detector. Due to the pressurized sensor cavity acoustic resonance phenomena degrade the oscillation behavior at certain operating frequencies. For sufficiently high Q-factors (> 50) the interrogation of the sensor using the SPDA and acoustic noise excitation shows a very good agreement with the reference method (laser vibrometer & optical excitation). Using a systematic frequency sweep during the "lock-in" detection the targeted temporal resolution of 1Hz cannot be achieved yet. Alternatively, pulse pair statistics can be used to process the demodulated image data of the SPDA (Meier et al. 2009, Miller et al. 1972). To implement this processing approach tests are currently ongoing where two SPDAs are operated in parallel with the same demodulation frequency. This technique is attractive as it can detect and analyze a complete range of frequencies without the need for a time consuming frequency sweep. Despite the averaging over several frames a temporal resolution of 1Hz should be attainable if the high frame rate of 5 kHz of the SPDA is considered.

References

Airaghi S (2006) Self-Illuminating Pressure Sensitive Paints Using Electroluminescent Foils. PhD Thesis ETH No. 16522, Swiss federal Institute of Technology (ETHZ), Zurich, Switzerland, 2006

Beer S, Seitz P (2005) Real-time tomographic imaging without x-rays: a smart pixel array with massively parallel signal processing for real-time optical coherence tomography performing close to the physical limits. Research in Microelectronics and Electronics, 2005 PhD, 2, pp. 135-138

Beltman W M, Van der Hoogt P J M, Spiering R M E J, Tijdeman H (1998) Implementation and experimental validation of a new viscothermal acoustic finite element for acousto-elastic problems. Journal of Sound Vibration 216(1), pp. 159-185

Blevins R D (1987) Formulas for natural frequency and mode shape, Robert E. Krieger Piblishing Co., Inc., ISBN 0-89874-791-0

Crocker J M (1998) Handbook of Acoustics. John Wiley & Sons, Inc., ISBN 0-471-25293-X (Chapter 10)

Fruehauf J (2005) Shape and Functional Elements of the Bulk Silicon Microtechnique, Springer, ISBN 3-540-22109-3

Helbert J N (2001) Handbook of VLSI microlithography: principles, technology and applications. William Andrew Inc., ISBN 0-8155-1444-1

Henning A K, Patel S, Selser M, Cozad B A (2004) Factors Affecting Silicon Membrane Burst Strength, Proc. of SPIE Vol. 5343, pp. 145-153

Lemmen R L C, Panuszka R J (1996) Numerical Evaluation of Acoustic Power Radiation and Radiation Efficiencies of Baffled Plates, In: V School Energy Methods in Vibroacoustics, 1996, Technical University of Mining and Metallurgy, Cracow ,Poland.

Liu T, Sullivan JP (2005) Pressure and Temperature Sensitive Paints. Springer, 2005, ISBN 3-540022241-3

Manthey W, Kroemer N, Magori V (1992) Ultrasonic transducers and transducer arrays for applications in air. Meas. Sci. Technol., (3): pp. 249-261, 1992

Prochazka L, Roesgen T (2005) Remote Sensing of Pressure Distributions on Aerodynamic Models. Technical Proposal, Institute of Fluid Dynamics (IFD), Swiss federal Institute of Technology (ETHZ), Zurich, Switzerland

Rafiq M, Wykes C (1991) The performance of capacitive ultrasonic transducers using v-grooved backplates. Meas. Sci. Technol., (2): pp. 168-174, 1991

Reimer K, Engelke R, Hofmann U, Merz P, Kohlmann-von Platen KT, Wagner B (1999) Progress in gray-tone lithography and replication techniques for different materials, Proceedings of SPIE, Vol. 3879, August 1999, pp.98-105

Sallese J M, Ills A, Bouvet D, Fazan P, Merritt C (2000) Modeling of the depletion of the amorphous-silicon surface during hemispherical grained silicon formation. J. Appl. Phys. 88 (10), November 2000, pp. 5751-5755

Stemme G (1991) Resonant silicon sensors, J. Micromech. Microeng, 1 (1991), pp. 113-125

Uttamchandani D, Thornton KEB, Nixon J, Culshaw B (1987) Optically excited resonant diaphragm pressure sensor, Electronics Letters, 23(4), 1987

Watanabe H, Nahomi A, Saburo A, Takamaro K (1991) Device application and structure observation for hemispherical-grained Si, J. Appl. Phys. 71 (7), April 1992, pp. 3538-3543

Wallace C E (1972) Radiation Resistance of a Rectangular Panel, J. Acoust. Soc. Amer. 51(3), (1972), pp. 946-952

Wu Z, Ma X, Brett P N, Xu J (2009) Vibration analysis of submerged rectangular microplates with distributed mass loading, Proc. R. Soc. A 2009 465, pp. 1323-1336